

RESEARCH ARTICLE

10.1002/2015JA022089

Generation of magnetosonic waves over a continuous spectrum

Lunjin Chen¹, Jicheng Sun², Quanming Lu², Xinliang Gao², Zhiyang Xia¹, and Zeren Zhima¹¹Department of Physics, University of Texas at Dallas, Richardson, Texas, USA, ²CAS Key Laboratory of Geospace Environment, Department of Geophysics and Planetary Science, University of Science and Technology of China, Hefei, China

Key Points:

- Proton ring distribution can cause discrete and continuous instability of perpendicular MS waves
- A condition for a discrete instability and a continuous instability is formulated
- PIC simulation results confirm the linear theory of continuous and discrete instability

Correspondence to:

L. Chen,
lunjin.chen@gmail.com

Citation:

Chen, L., J. Sun, Q. Lu, X. Gao, Z. Xia, and Z. Zhima (2016), Generation of magnetosonic waves over a continuous spectrum, *J. Geophys. Res. Space Physics*, 121, 1137–1147, doi:10.1002/2015JA022089.

Received 28 OCT 2015

Accepted 28 DEC 2015

Accepted article online 8 JAN 2016

Published online 5 FEB 2016

Abstract Magnetosonic waves, also known as equatorial noise emission, were found to have discrete frequency structures, which is consistent with instability caused by proton ring distribution. Nonetheless, nondiscrete structure, i.e., a broadband spectrum over a continuous frequency range, has been reported. We investigate the question whether proton ring distribution can generate nondiscrete spectra for perpendicularly propagating magnetosonic waves. We propose discrete and nondiscrete characteristics of the local instability for explaining the observation of discrete, continuous, and mixed spectra. The criterion for transition from discrete and continuous instability is given, $\gamma > \sim \Omega_p/2$, where γ is wave growth rate and Ω_p is proton cyclotron frequency. The condition is verified by particle-in-cell simulation using more realistic electron-to-proton mass ratio and speed of light than in previous studies. Such criterion of generating a continuous spectrum can be tested against simultaneous in situ measurement of wave and particle. We also find that the modes at low Ω_p harmonics, including the fundamental Ω_p , can be still excited through nonlinear wave-wave coupling, even when they are neutral modes ($\gamma = 0$) according to the linear kinetic theory. Comparison with magnetosonic waves in cold plasma limit and electromagnetic ion Bernstein mode is also discussed.

1. Introduction

Fast magnetosonic (MS) waves, also known as equatorial noise, occur at frequencies from a few hertz to several hundreds of hertz and are primarily confined within a few degrees from the geomagnetic equator [Russell *et al.*, 1970; Gurnett, 1976; Olsen *et al.*, 1987; Santolík *et al.*, 2002; Němec *et al.*, 2005; Tsurutani *et al.*, 2014] both inside and outside the plasmopause. It has been suggested observationally [e.g., Perraut *et al.*, 1982; Boardsen *et al.*, 1992; Meredith *et al.*, 2008; Balikhin *et al.*, 2015] and theoretically [e.g., Curtis and Wu, 1979; Horne *et al.*, 2000; Chen *et al.*, 2010; Liu *et al.*, 2011; Gary *et al.*, 2010] that such equatorial MS waves can be excited with wave vectors nearly perpendicular with respect to the background magnetic field, by a natural instability associated with a ring distribution ($\partial f/\partial v_\perp > 0$) of energetic protons at energies of the order of 10 keV. It is interesting to note that magnetosonic waves, although low in intensity, can occasionally be detected as far as 50° away from the magnetic equator [Tsurutani *et al.*, 2014].

The magnetosonic waves have received increasing attention recently due to their roles in scattering energetic electrons in the magnetosphere. It has been shown that these waves are capable of scattering energetic electrons through Landau resonance interaction [Horne *et al.*, 2007; Li *et al.*, 2014]. MS waves with amplitude ~ 200 pT can provide acceleration of MeV electrons over a time scale of ~ 1 day, which is comparable to that of the generally accepted dominant acceleration mechanism due to cyclotron resonance with whistler mode chorus emission [Horne *et al.*, 2005; Thorne *et al.*, 2013]. Additional transit time scattering of energetic electrons arises due to spatial confinement of MS waves near the equator [Bortnik and Thorne, 2010]. Chen *et al.* [2015] recently demonstrated that MS waves can be in bounce resonance with equatorially mirroring electrons, which are, in general, immune to gyroresonance interaction. The bounce resonance is capable of kicking those electrons out of the equatorial plane, making subsequent scattering due to other waves possible. The electron scattering due to the bounce resonance is later quantified by Li *et al.* [2015]. Xiao *et al.* [2015] present a case where combined acceleration due to magnetosonic waves and chorus waves can be responsible for the formation of electron butterfly distribution in the inner magnetosphere.

Since its first report in the 1970s, equatorial noise has been known to consist of many discrete spectral lines with nearly equal spacing, which were later related to multiples of proton gyrofrequencies (Ω_h). This discrete spectral property is reproduced by an instability driven by proton ring free energy via harmonic cyclotron resonance instability [e.g., *Gulelmi et al.*, 1975]. To resolve harmonic structure of the MS wave observation, one requires a waveform sampling rate of at least a few proton gyrofrequencies to capture the MS wave frequency and also requires collection of waveform data over a time period of at least a few gyration periods of protons (typically on the order of several seconds) to ensure sufficient frequency resolution in the spectral analysis (e.g., Fourier transformation). The sampling frequency and the collection time of the waveform are constrained by satellite telemetry, and thus, the detection of MS harmonic lines, if any, is not always available. Spectral analysis on the waveform by previous studies has demonstrated many examples of discrete structures of MS waves. For example, magnetic fluctuation continuously recorded on board GEOS with sampling frequency of ~ 23 Hz [*Perraut et al.*, 1982] showed the first few harmonic frequencies below ~ 11.6 Hz (Nyquist frequency). Higher discrete harmonics are also evident from *Gurnett* [1976]. Recently, *Fu et al.* [2014], *Boardsen et al.* [2014], and *Němec et al.* [2015b], using Time History of Events and Macroscale Interactions during Substorms, Van Allen Probes, and Cluster observations, respectively, reveal that MS wave intensity exhibits quasiperiodic modulation with period about several minutes in a time-frequency dynamic spectrum and that some of the modulated elements exhibit chorus-like rising tone (rising frequency with time) with a rate of ~ 1 Hz/s. Although discrete natures were not discussed in the rising tone events reported in the former two studies, *Němec et al.* [2015b] confirmed that the rising tone spectra are also made of discrete lines and that frequency spacing between discrete lines is about Ω_h .

Nonetheless, discrete spectra are not always observed. *Tsurutani et al.* [2014] report a MS wave event during an equatorial crossing. Interestingly, spectral analysis of the corresponding coincident waveforms yields no discrete structures, and the obtained spectrum is continuous as a function of frequency instead. The lack of harmonic structure, as pointed out by the authors, is unlikely due to either sampling frequency or waveform time duration limitations. A mixture of discrete spectra and nondiscrete spectra is also evident in Figure 4 of *Gurnett* [1976]. The question arises, "What dictates discrete or continuous nature of MS waves?" In this study we will focus on the generation of discrete and continuous spectra, specifically, whether MS waves can be generated over a broad range of continuous frequencies by a proton ring distribution. We will explore, for the first time, the condition of generating a broadband spectrum of MS waves. Here is the organization of the paper. In section 2, a theoretical investigation of the formation of broadband MS waves due to a proton ring distribution is given based on the linear dispersion relation for the perpendicular propagation. The criterion for generating discrete and continuous frequency spectra is provided. Corresponding particle-in-cell (PIC) simulations are also performed in section 3 to verify the linear theory, followed by conclusions and discussion in section 4.

2. Linear Theory

To examine conditions for generating a continuous frequency spectrum of MS waves, we assume a uniform and magnetized plasma consisting of three components, cold electron, cold proton, and hot proton components, whose number densities are denoted by N_e , N_{ch} , and N_{hh} and satisfy charge neutrality ($N_e = N_{ch} + N_{hh}$). The hot proton component is modeled with an ideal ring distribution,

$$f_{hh} = N_{hh} \delta(v_{\parallel}) \delta(v_{\perp} - V_R) / (2\pi v_{\perp}), \quad (1)$$

where v_{\parallel} and v_{\perp} are velocities parallel and perpendicular to the background magnetic field \mathbf{B}_0 and V_R is the proton ring velocity.

The kinetic dispersion relation of the extraordinary mode for perpendicular propagation can be written as

$$D(\omega, k) = \epsilon_{xx}(\epsilon_{yy} - n^2) + \epsilon_{xy}^2 = 0, \quad (2)$$

where $n = kc/\omega$, ω is complex frequency, k is perpendicular wave number, and $c = 1/\sqrt{\mu_0\epsilon_0}$ is the speed of light (ϵ_0 is the vacuum permittivity and μ_0 is the vacuum permeability). Double subscripts denote the elements of dielectric tensor ϵ , where subscript x represents the direction of wave vector \mathbf{k} ($\perp \mathbf{B}_0$) and

y completes right-handed orthogonal coordinate systems with z along \mathbf{B}_0 . The above three components of ϵ for the modeled three-species plasma can be expressed as

$$\begin{aligned}\epsilon_{xx} &= 1 + \frac{\omega_{pe}^2}{\Omega_e^2 - \omega^2} + \frac{\omega_{pch}^2}{\Omega_h^2 - \omega^2} + \frac{\omega_{phh}^2}{\omega^2} \left(-1 + \sum_n \frac{n2n^2 J_n(\lambda) J_n'(\lambda)}{n - \omega/\Omega_h} \right) \\ \epsilon_{xy} &= \frac{i\omega_{pe}^2 \Omega_e}{(\Omega_e^2 - \omega^2)\omega} + \frac{i\omega_{pch}^2 \Omega_h}{(\Omega_h^2 - \omega^2)\omega} + \frac{\omega_{phh}^2}{\omega^2} \sum_n \frac{in^2 [J_n'(\lambda)^2 + J_n(\lambda) J_n''(\lambda)/\lambda + J_n(\lambda) J_n''(\lambda)]}{n - \omega/\Omega_h} \\ \epsilon_{yy} &= 1 + \frac{\omega_{pe}^2}{\Omega_e^2 - \omega^2} + \frac{\omega_{pch}^2}{\Omega_h^2 - \omega^2} + \frac{\omega_{phh}^2}{\omega^2} \left(-1 + \sum_n \frac{n2J_n'(\lambda)(J_n'(\lambda) + \lambda J_n''(\lambda))}{n - \omega/\Omega_h} \right),\end{aligned}\quad (3)$$

where electron gyrofrequency $\Omega_e = -eB_0/m_e$, proton gyrofrequency $\Omega_h = eB_0/m_h$, $\omega_{pe}^2 = N_e e^2/(\epsilon_0 m_e)$, $\omega_{pch}^2 = N_{ch} e^2/(\epsilon_0 m_h)$, $\omega_{phh}^2 = N_{hh} e^2/(\epsilon_0 m_h)$, m_e and m_h are the electron and the proton masses, respectively, e is elementary charge, and the argument of Bessel functions $\lambda = kV_R/\Omega_h$. The values of 1 in equation (3) originate from the displacement current, and the last three terms on the right-hand sides denote contributions from the cold electron, cold proton, and hot proton ring components, respectively.

Given plasma parameters, \mathbf{B}_0 and k , equation (2) can be solved for complex frequency ω , whose real part ω_r is the real wave frequency and whose imaginary part γ is the temporal growth rate (positive for growth and negative for damping). Note that this dispersion relation is also called “generalized” electromagnetic ion Bernstein modes with appreciable y component of wave electric field perpendicular to the wave vector \mathbf{k} (i.e., x direction). In the electrostatic limit ($\mathbf{E}/|\mathbf{k}$, i.e., $|E_x| \gg |E_y|$), the dispersion relation can be approximated by $\mathbf{k} \cdot \epsilon \cdot \mathbf{k} = 0$ (i.e., $\epsilon_{xx} = 0$) [e.g., *Bernstein*, 1958]. In our paper we do not make such approximation, and the electromagnetic dispersion relation is used. It should be noted that the cold plasma limit of generalized electromagnetic ion Bernstein modes, i.e., the limit of $\lambda \rightarrow 0$ in equations (2) and (3), is the extraordinary mode (or magnetosonic wave mode) below the lower hybrid resonance frequency, while there is no corresponding cold plasma limit for the electrostatic waves except at lower hybrid resonance frequency.

For magnetosonic wave modes considered, there exist multiple solutions of complex wave frequency for a given k . A characteristic of perpendicular instability, where k_z vanishes, is that only conjugate complex frequency pair (growth and damping mode) and neutral mode ($\gamma = 0$) are allowed. Neutral mode solutions can be found by the contour of $D(\omega, k) = 0$ with ω and k being real numbers. As for unstable modes $\gamma > 0$, we search all possible solutions for a given k in the complex frequency domain with $10^{-3} \leq \gamma/\Omega_h \leq 1$ and $1.5 \leq \omega_r/\Omega_h \leq 40$. This root finding method ensures that all the complex frequency solutions within this domain will be identified for a given k , and this procedure is repeated for each k from $0.1k_0$ to $50k_0$ with a spacing $0.02k_0$, where $k_0 = \Omega_h/V_A$. V_A here is Alfvénic speed, defined as $B_0/\sqrt{\mu_0 N_e m_h}$. Such high-resolution k array is adopted because unstable modes may localize over a narrow range of k and ω .

The black lines in Figure 1a show the neutral mode solutions with $V_R/V_A = 1$ and the hot proton fraction $\eta_{hh} = 0.8\%$ (N_{hh}/N_e). We adopt $N_e = 6.15 \text{ cm}^{-3}$ and $B_0 = 248 \text{ nT}$ (corresponding to L -shell = 5 for the dipole field). The neutral modes exhibit similar structures to neutral modes of ion Bernstein mode structure in a Maxwellian plasma [*Fredricks*, 1968]. There exist multiple-frequency branches separated by $n\Omega_h$, where n is a positive integer, with resonances ($k = \infty$) and cutoffs ($k = 0$) near the frequencies $n\Omega_h$. Although the neutral ion Bernstein modes are distinct from the cold plasma dispersion curve of the magnetosonic waves (the solid magenta line), the envelope of the relatively steeply sloped regions in each neutral mode branch can be approximately traced by the cold magnetosonic wave dispersion curve. Unlike a Maxwellian plasma, proton ring distribution permits unstable mode solutions, which are traced by colored line segments with color representing the value of γ (greater positive γ in red and zero values in blue). The corresponding γ is also plotted in Figure 1b. The cold dispersion curve of the magnetosonic waves also traces well the unstable mode solutions, which is expected because of cold species-dominant plasma with a small fraction of hot proton component. As shown clearly in an expanded plot in the lower right corner of Figure 1a, unstable modes occur only at gaps separating steep slopes of neighboring neutral mode branches, with peak growth rates at the centers of the gaps (near $n\Omega_h$) and zero growth rates near the neutral mode branches (black lines). As a consequence the growth rate profile shows discrete peaks at $n\Omega_h$, and γ vanishes when away from $n\Omega_h$ (Figure 1b).

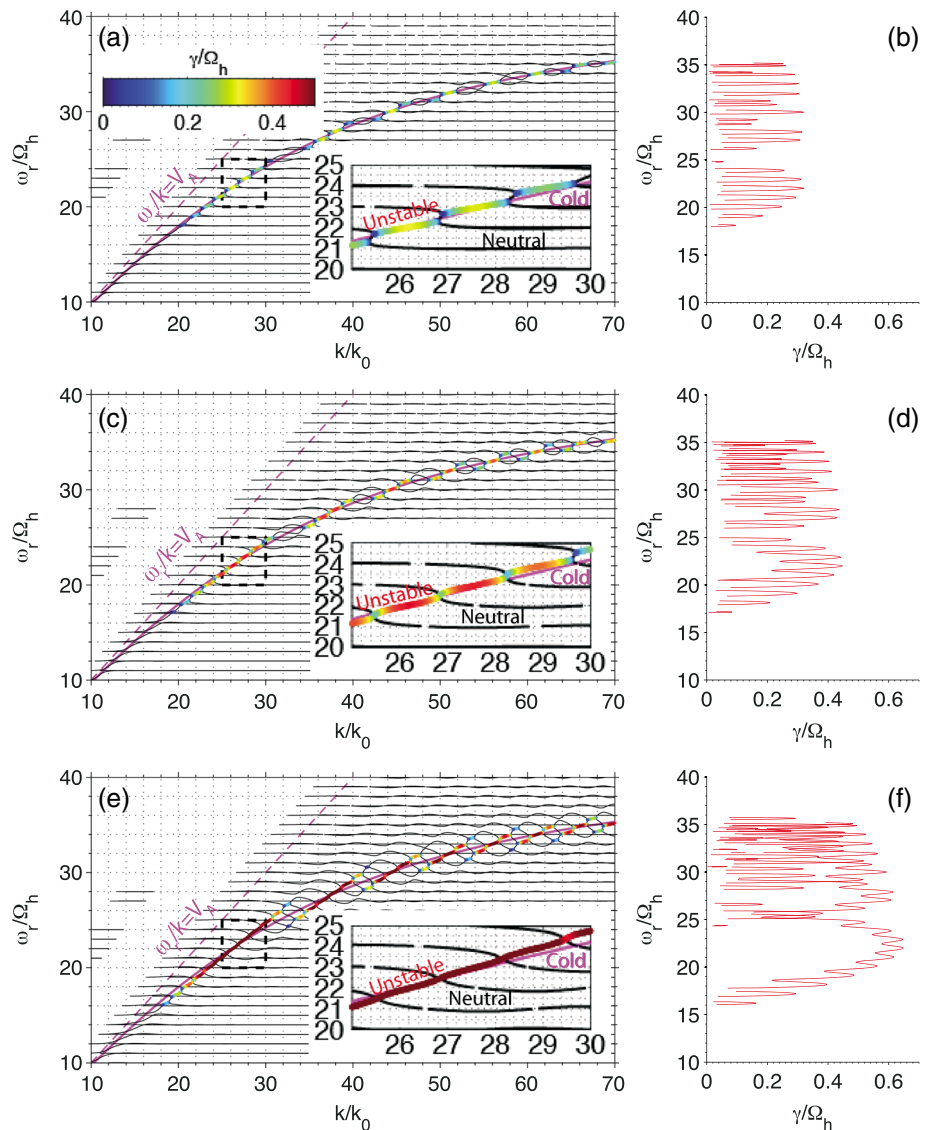


Figure 1. Dispersion relation of perpendicular MS waves. Normalized wave frequency (ω_r/Ω_h) (a) versus normalized wave number k/k_0 for $V_R/V_A = 1$ and $\eta_{hh} = 0.8\%$ and (b) versus normalized growth rate γ/Ω_h . The black lines in Figure 1a denote neutral mode solutions, the solid magenta line denotes corresponding cold plasma solution, and the dashed magenta line denotes $\omega/k = V_A$. An expanded plot of the dashed rectangular region is shown in the lower right corner of the plot. Colored line segments represent unstable solutions ($\gamma > 0$), with corresponding γ color coded. Corresponding γ of unstable solutions is also shown versus wave frequency ω_r in Figure 1b. Similar to Figures 1a and 1b but (c and d) for $\eta_{hh} = 1\%$ and (e and f) for $\eta_{hh} = 3\%$.

Dispersion relation solutions for higher values of η_{hh} are shown in Figures 1c and 1d for $\eta_{hh} = 1\%$ and Figures 1e and 1f for $\eta_{hh} = 3\%$. As η_{hh} increases, the increased thermal correction of hot proton component influences the real part of dispersion relation, i.e., the curves of ω_r versus k , by broadening the regime having steep slopes. For $\eta_{hh} = 1\%$, the cold dispersion relation still traces well with unstable modes, and thus, the peak growth rates scale well with η_{hh} . This can be seen by comparing the maximum growth rates in Figures 1d and 1b. The ratio of the two maximum growth rates (~ 1.35) is close to the ratio of η_{hh} values ($= 1.25$). The discrete growth rate profile is also clearly seen for $\eta_{hh} = 1\%$ in Figure 1d. For $\eta_{hh} = 3\%$, however, there are a few noticeable changes. First, the thermal correction of hot proton component broadens further the region of steep slopes for the neutral modes so that the unstable mode solutions deviate from the trace of the cold dispersion curve. Second, the growth rate increases with increasing η_{hh} , but because of the deviation from the cold dispersion curve, the growth rate profile does not scale linearly with η_{hh} , which is readily seen by comparing the

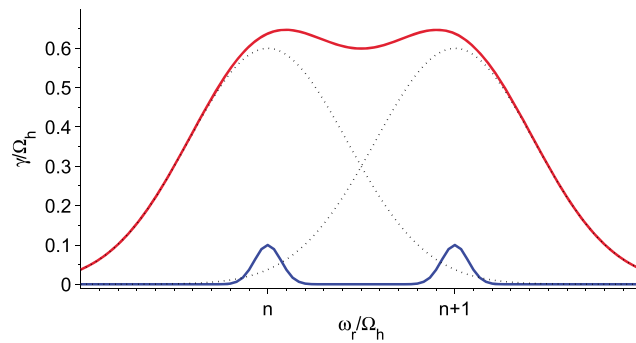


Figure 2. Illustration of two weak growth rate peaks leading to a two-peak profile (blue line) and two strong growth rate peaks (black dotted lines) merging to a continuous profile (red line).

maximum growth rate with those for the previous two η_{hh} values. Third, the instability can sometimes peak in between instead of exactly at proton gyrofrequency harmonics $n\Omega_h$, and the frequency spacing between discrete peaks can deviate from $1\Omega_h$ by up to a fraction of Ω_h . Fourth, the growth rate profile for $\eta_{hh} = 3\%$ exhibits a mixture of discrete peaks separated by neutral mode ($\gamma = 0$) and continuous structures with continuous positive γ , crossing several proton gyrofrequency harmonics. The discrete structures tend to occur when γ is small, while the continuous structures favor greater γ . The continuous structures with continuous positive γ are clearly seen in the expanded plot in the lower right corner of Figure 1e. As pointed out previously [e.g., Gulemi et al., 1975; Chen, 2015], the frequency width of a discrete growth rate peak is on the order of the corresponding peak growth rate. Because of this property, the continuous structures can be interpreted

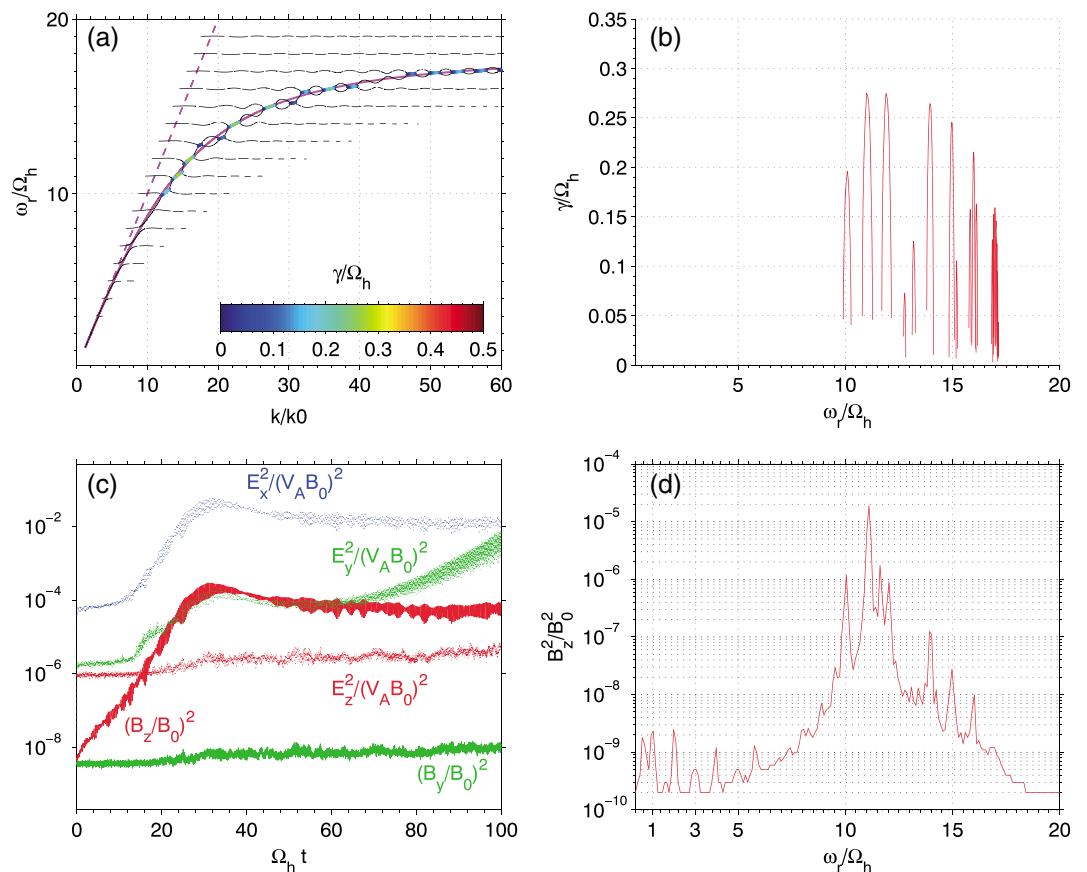


Figure 3. (a, b) Dispersion relation in a similar format as Figure 1, corresponding to parameters used in PIC Run 1, $V_R/V_A = 1$, $\eta_{hh} = 0.3\%$, $m_e = m_h/1600$, and $c/V_A = 20$. (c) Time evolutions of spatially averaged wave energy for electromagnetic fields from PIC Run 1 and (d) power spectral intensity of wave B_z component.

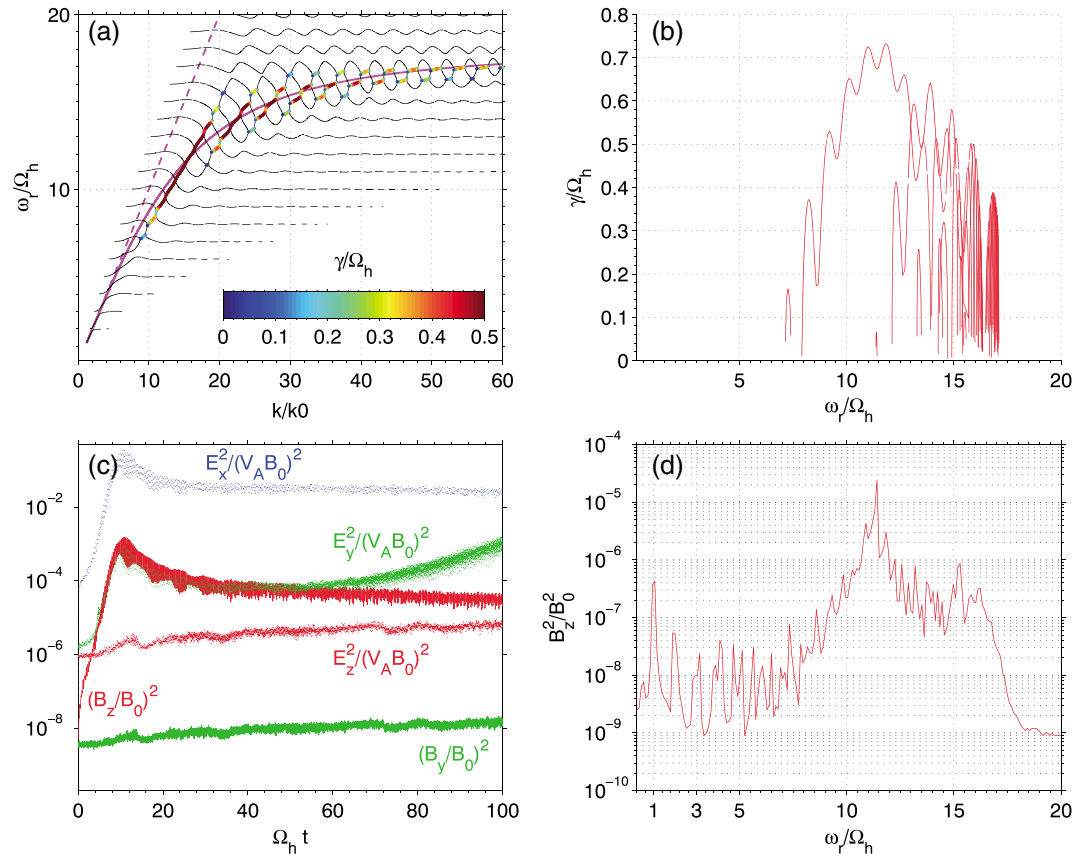


Figure 4. The same as Figure 3 except for PIC Run 2 with $\eta_{hh} = 2\%$.

as merging of growth rate peaks, as illustrated in Figure 2. When two neighboring growth rate peaks have small peak values near $n\Omega_h$, the two peaks are well separated, resulting in a discrete structure. In contrast, when two neighboring growth rate peaks have sufficient large peak values so that the frequency width of peaks are comparable to the frequency separation of the two peaks ($1\Omega_h$), the two peaks merge and result in a continuous γ profile without a gap of $\gamma = 0$. Therefore, one can propose a criterion for the formation of continuous structures, peak growth rate $\gamma_{peak} > \sim 0.5\Omega_h$. As shown in Figure 1f, continuous structures occur when this criterion is satisfied, while pronounced discrete peak structures occur for the smaller γ (Figures 1b and 1d).

3. Particle-In-Cell Simulation

To verify the linear theory about the generation of discrete and continuous structures, 1-D electromagnetic particle-in-cell (PIC) simulation is performed in a uniform magnetized plasma. The code has been successfully used in *Lu et al.* [2010]. Consistent with the coordinate system defined for the linear theory in section 2, we use x for the direction of the variation for wave electromagnetic field and z for the direction of the background magnetic field, and y completes the right-handed coordinate system. Periodic boundary conditions are used in our simulation model. The 8192 x grid cells are used, and grid cell size $\Delta x = 0.75 \times 10^{-3} V_A / \Omega_h$, which is $\sim 2.4 \lambda_D$ (λ_D is plasma Debye length). There is an average of 60 macroparticles in every cell for each species. The time step is $\Delta t = 0.25 \times 10^{-4} \Omega_h^{-1}$, and the simulation is run for $t = 100 \Omega_h^{-1}$. To ensure the stability of the code, the time step must satisfy the Courant condition $\Delta t < \Delta x / c$. The computation time of a PIC simulation increases with the number of macroparticles and the number of time steps, which are determined by the grid cell size Δx and the time step Δt , respectively. For PIC simulation with the fixed simulation box and simulation time, the larger light speed c requires smaller Δx and smaller Δt , which ultimately results in more macroparticles and more time steps.

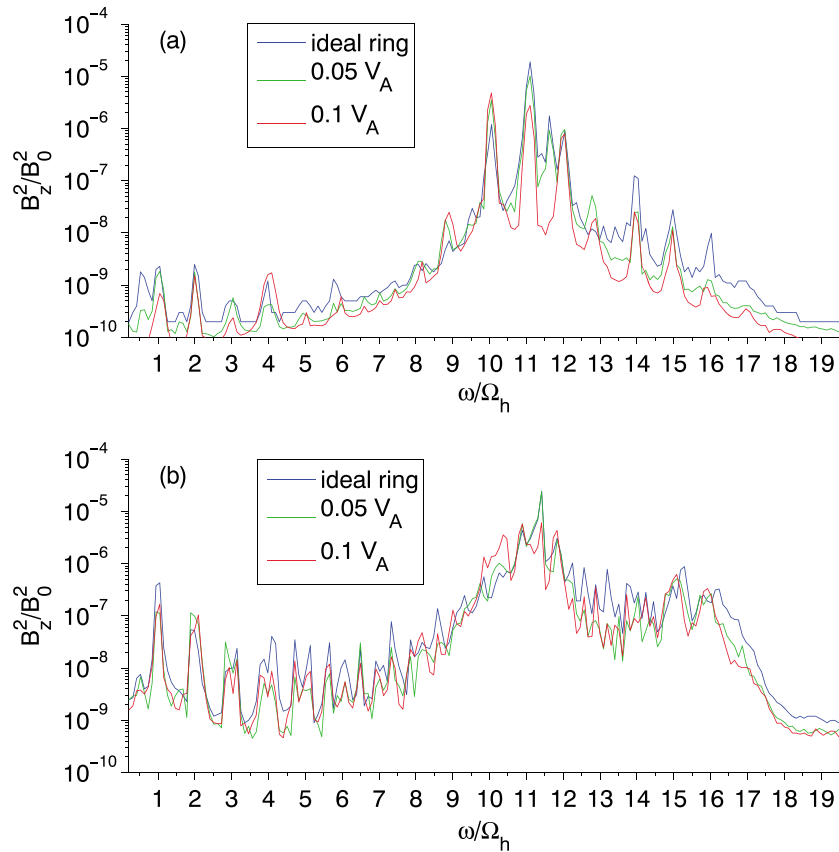


Figure 5. The effect on simulated wave B_z power spectral intensity due to different proton ring thermal spreading for (a) $\eta_{hh} = 0.3\%$ and (b) $\eta_{hh} = 2\%$. The thermal spreadings $V_{th} = V_A$ (i.e., ideal rings), $0.05V_A$, and $0.1V_A$ are considered and are denoted by blue, green, and red lines, respectively.

Considering the computation time constraint, we use slightly heavier electron mass $m_e = m_h/1600$ and relatively low value of $c = 20V_A$ for the PIC simulation. PIC simulation is set up in a plasma consisting of three components as section 2, cold electron (1 eV), cold proton (1 eV), and a hot proton ring component ($V_R = V_A$). Because of the modification of m_e and c , the dispersion relations for the three representative η_{hh} cases shown in Figure 1 do not have PIC simulation counterparts. In this section, we run two representative cases, with $\eta_{hh} = 0.3\%$ and 2% , respectively, to show the comparison of PIC simulation and linear kinetic theory. Figures 3a and 3b show dispersion relation for $\eta_{hh} = 0.3\%$ in the format similar to Figure 1, with the modified m_e and c (through ϵ_0 modification) in equations (2) and (3). Just as in Figures 1a and 1b, the unstable mode is well traced by the cold dispersion curve (the magnet solid line), and, because the growth rate is small ($\gamma < 0.3\Omega_h$), the growth rate profile shows discrete peaks at $10, 11, \dots, \text{and } 17\Omega_h$. Figure 3c shows spatially averaged wave electric and magnetic field as a function of time normalized to $1/\Omega_h$. Linear growth occurs initially with exponential increases in wave electric and magnetic field strength before saturation at $\Omega_h t \sim 30$. The saturated wave has dominant field-aligned magnetic component B_z , showing a wave compressional nature, and dominant electric field component along wave vector and another appreciable component in y direction. Fourier transform of dominant magnetic field B_z time series over $100\Omega_h t$ is performed, and the produced spatially averaged power spectral density is shown in Figure 3d. The power spectral density shows discrete peaks at harmonic frequencies from 10 to $17\Omega_h$, with a minimum power near $13\Omega_h$. These discrete spectral peaks are consistent with the growth rate profile obtained from the linear theory (Figure 3b).

Another PIC simulation, Run 2, is set up with the same parameters except using higher $\eta_{hh} = 2\%$. Figures 4a and 4b show corresponding linear dispersion relation and Figures 4c and 4d show PIC simulation results. The unstable mode dispersion relation (colored line segments) deviates from the cold plasma dispersion curve (the solid magenta line) because of thermal correction from the hot proton component. Linear growth rate reaches a maximum value of $\sim 0.7\Omega_h$ near $11-12\Omega_h$, leading to a continuous growth rate profile as a func-

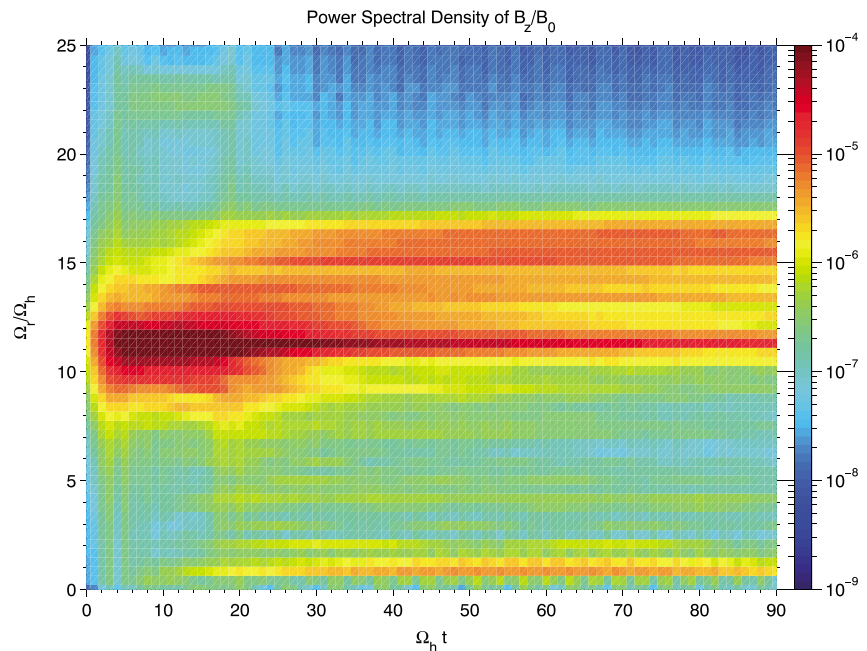


Figure 6. Power spectral density of B_z/B_0 , obtained from windowed Fourier transform, for PIC Run 2 as a function of normalized frequency and time.

tion of frequency. Wave electric and magnetic field from the PIC simulation Run 2 reaches saturation near $10\Omega_h t$, earlier than Run 1, because of greater free energy available and a greater exponential growth rate. Saturated wave electric and magnetic field show similar features as Run 1 in that magnetic compressional component B_z is dominant and electric field is predominantly along the direction of wave vector. The Fourier power spectral density of B_z (Figure 4d) shows a continuous profile with peak near $11.5\Omega_h$ and with pronounced peak from 10 to $15\Omega_h$, which is consistent with results from the linear theory (Figure 4b). Moderate peak structures are also seen near $16\Omega_h$ and below $8\Omega_h$, where the linear growth rate is small.

Ideal proton ring distributions, i.e., δ functions in equation (1) with zero thermal spreading of proton ring distribution $V_{th} = 0$, are used in the previous two simulation runs. Here we examine the dependence of PIC simulation results on V_{th} . Figure 5a shows power spectral intensity of wave B_z components for Run 1 (the case of low $\eta_{hh} = 0.3\%$) except with changing thermal spread V_{th} , $V_{th} = 0$ (ideal rings in the blue line), $V_{th} = 0.05V_A$ (in the green line), and $V_{th} = 0.1V_A$ (in the red line). PIC simulations are also performed for Run 2 (the case of high $\eta_{hh} = 2\%$) with varying V_{th} shown in Figure 5b in the format similar to Figure 5a. The simulations with different V_{th} values produce comparable overall profiles of the power spectral intensity. The increasing thermal spreading seems not to blur the discrete emission in Figure 5a and produces little change on the continuous spectra in Figure 5b too. From eye inspection, the power spectral intensity for the largest V_{th} in the red line of Figure 5a seems to have clearer spectral peaks than the lower V_{th} cases, which might be due to the reduction in the growth rate of perpendicular waves when proton ring distribution smooths out.

We note that the low harmonics below $\sim 7\Omega_h$ are visible in the power spectral density from PIC simulation (Figures 3d, 4d, and 5), while linear kinetic theory predicts neutral mode with zero growth rate for those frequencies (Figures 3b and 4b). Figure 6 shows spatially averaged power spectral density of B_z/B_0 for PIC Run 2 as a function of normalized frequency and time. The power spectral density is obtained from windowed Fourier transform with time window size of $15\Omega_h^{-1}$ and time shift of $1\Omega_h^{-1}$. The choice of such a large window size ($15\Omega_h^{-1}$) ensures sufficient frequency resolution in order to resolve the harmonic lines. One can notice the development of the lower harmonics ($< \sim 7\Omega_h$), beside the excitation of waves in the frequency range ($8-17\Omega_h$) predicted by the linear kinetic theory. Wave intensity at Ω_h is greater than at $2\Omega_h$, which is greater than other harmonics for $\omega_r < 7\Omega_h$, and the wave at Ω_h develops earlier than at $2\Omega_h$, which is earlier than other harmonics for $\omega_r < 7\Omega_h$. The higher intensity and earlier development at Ω_h supports that nonlinear wave-wave resonance is involved in the excitation at the fundamental and low harmonics, whose linear growth rate is 0 according to linear theory. As *Perraut et al.* [1982] points out, perpendicular magnetosonic

waves lie on or close to the “linear” dispersion relation, $\omega = kV_A$, which favors strong mode-mode coupling. The conditions for mode coupling can be automatically satisfied, $k_1 \pm k_2 = k_{\pm}$, $\omega_1 \pm \omega_2 = \omega_{\pm}$, and $D(\omega_{\pm}, k_{\pm}) = 0$, provided that $D(\omega_1, k_1) = 0$ and $D(\omega_2, k_2) = 0$. Take as example $\omega_1 = 10\Omega_h$ and $\omega_2 = 11\Omega_h$, which lie in the unstable frequency range (Figure 4). Beating of the two waves leads to the excitation at the frequency difference, that is, the fundamental frequency Ω_h . The excitation at the frequency sum, although weaker, is also visible near $\sim 21\Omega_h$ for $\Omega_h t < \sim 20$, which supports the wave-wave resonance process. The generation of the fundamental can further nonlinearly excite the harmonics above the fundamental. For weaker instability such as the case of PIC Run 1 where harmonic emission can be excited, similar processes can occur. Furthermore, for weaker instability the low harmonics at $n\Omega_h$ (where n is small positive integer, 1, 2, ...) can be also excited directly through beating of two unstable waves whose frequency difference matches n . This argument seems consistent with Figure 5a where wave intensity at 2 and 4 Ω_h is comparable to or even stronger than the fundamental. Detailed analysis on the nonlinear process is beyond the scope of our current study on discrete and continuous instability and will be pursued in the future.

4. Conclusions and Discussion

We investigate the question whether perpendicular MS wave can be unstable over a broad range of continuous frequencies by proton ring distributions. The question is addressed using a combination of linear theory and PIC simulations, and the criterion for discrete and continuous instability transition is proposed. Our principal conclusions are summarized as follows:

1. Proton ring distribution can cause an instability generating discrete wave bands and another generating continuous wave bands. Generation of a continuous frequency spectrum of MS waves can be explained as emergence of neighboring discrete peaks.
2. A condition for a discrete instability and a continuous instability is formulated. The former occurs when growth rate is small $\gamma < 0.5\Omega_h$, while the latter occurs when growth rate is comparable to or above $0.5\Omega_h$.
3. PIC simulation results confirm the linear theory on generation of continuous frequency spectrum and discrete frequency spectrum.

Discrete and continuous instabilities occurring at perpendicular propagation also occur at smaller wave normal angles with finite k_{\parallel} value [Chen, 2015] but for different physical explanations. For the latter case of not exactly perpendicular propagation, discrete instability favors small value k_{\parallel} , by which only a single resonant interaction is in effect and only near proton gyrofrequency harmonics, while continuous instability is caused by contributions of multiple harmonic resonant interactions when k_{\parallel} increases. For the former case of perpendicular propagation, instability is nonresonant and protons of any v_{\parallel} contribute to the instability. When instability is weak, the instability occurs at discrete frequencies (i.e., harmonic proton gyrofrequency). When growth rate γ becomes comparable to or greater than $\Omega_h/2$, the frequency spreading near proton cyclotron frequency harmonics is wide and thus instability can occur over a continuous frequency range. While the discrete and continuous instabilities for finite k_{\parallel} value depend on the value of k_{\parallel} , regardless of the growth rate, the discrete and continuous instabilities for perpendicular direction depend on the value of γ . It should also be noted that growth rate may peak at frequencies in between harmonics of Ω_h (e.g., Figures 1d and 1f).

The criterion for discrete and continuous instabilities at the perpendicular direction depends on the value of γ and is rather generic, independent of the proton ring assumption made. The effect of proton ring thermal spread seems not to affect such criterion either (as shown in Figure 5). Growth rate of MS waves depends on several factors [Chen *et al.*, 2010]; strong growth rate is favored when V_R/V_A is near 1, when the number density for proton ring distribution increases, and when cold plasma density (or f_{pe}/f_{ce}) is low. One may expect higher probability of continuous spectra during storm times when energetic protons are freshly injected than during quiet times, and higher probability in the low-density trough than inside the high-density plasmasphere. The role of γ on discrete and continuous instabilities might be tested because only local measurements—local measurements of background plasma parameters, waveform, and proton distribution measurements (e.g., from Van Allen Probes)—are required for testing.

There are other possibilities for explaining the lack of harmonic spectra of magnetosonic waves reported [e.g., Tsurutani *et al.*, 2014]. One credible possibility is through wave propagation [Santolík *et al.*, 2002], through which harmonic emissions locally generated from a broad source region having different local proton gyrofrequencies lead to the blurring of the harmonic lines. Figure 7 illustrates such effect. A source region of size ΔL

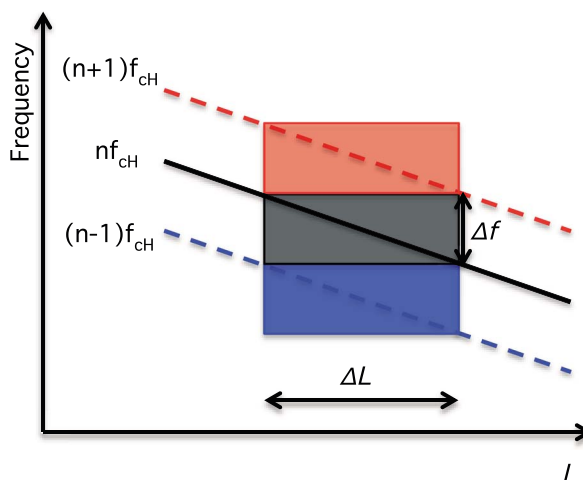


Figure 7. Illustration of broadening magnetosonic wave spectra due to a fine-size wave source region. f_{cH} denotes the local proton gyrofrequency.

contains many source points, with each producing harmonic emissions at harmonics of local proton gyrofrequency f_{cH} . Subsequent propagation near the equatorial plane leads to the broadening of, for example, the n th harmonic line with frequency spreading Δf . When Δf is greater than the harmonic spacing f_{cH} , the discrete spectrum vanishes and a continuous spectrum forms. One can estimate the size of the source region ΔL for forming a continuous spectra using $\Delta f > f_{cH}$, where Δf is related to ΔL , $\Delta f \approx n\Delta f_{cH}$. ΔL can therefore be determined through $\Delta f_{cH}/f_{cH} > 1/n$, which translates to $\Delta L/L > 1/(3n)$ for a dipole magnetic field. One can use $n = 10$ as a typical magnetosonic wave frequency [e.g., *Boardsen et al., 1992; Horne et al., 2007*] and $L = 5$ for a typical wave observation location [e.g., *Ma et al., 2013*] to obtain an estimate $\Delta L > 1/6$. This minimum size in L for a continuous spectrum is comparable with observations of a size of a MS emission source region. For example, the source region estimated from multiple-spacecraft Cluster observation ΔL is at least 0.15–0.2 [*Němec et al., 2015a, Figure 1; Němec et al., 2015b, Figures 1 and 2*] and can reach beyond 0.4–0.7 [*Němec et al., 2005, Figure 8*]. These estimates support the possibility that magnetosonic wave propagation to the observation point from different parts of the source region is capable of merging magnetosonic discrete lines into a continuous spectrum. It should be noted that wave propagation does not necessarily result in a continuous spectrum. The observation of a discrete MS wave event with frequency spacing not exactly at but near the equatorial proton gyrofrequency [e.g., *Perraut et al., 1982*] can be explained by the wave propagation, when the source region size is narrow. Recently, *Zhima et al. [2015]* report a discrete magnetosonic emission off the equator (at geomagnetic latitude $\sim -17^\circ$) and attribute the preservation of wave discrete nature to the wave propagation, where only waves from spatially narrow equatorial sources can access such high latitude.

Another possibility is through fine-scale rising tone spectra of magnetosonic waves recently reported [*Fu et al., 2014; Boardsen et al., 2014; Němec et al., 2015b*]. Isolated magnetosonic wave elements occur with a large spread in frequencies, which varies with time. In the presence of such varying frequency elements, a continuous spectrum can likely form if the elements from neighboring L shells merge to the observation location through propagation. This mechanism has less strict requirement on the minimum spatial size of the source region than the mechanism discussed above.

Nonetheless, the question for the formation of a continuous magnetosonic wave spectrum is interesting and deserves more investigation. Our proposed scenario for explaining the lack of discrete lines through local instability in the source region requires that $\gamma > \sim \Omega_h/2$. Although this scenario does not exclude other possibilities, it might be tested against the local observation to provide more insight for the understanding of magnetosonic wave instability. This will be left as a future study.

Acknowledgments

No observational data are analyzed in the paper. This research was supported by the NSF grant AGS-140504. The work at USTC was supported by the National Science Foundation of China, grants 41331067, 41474125, 41174124, and 11235009. The authors would like to acknowledge the two reviewers for their helpful suggestions.

References

Balikhin, M. A., Y. Y. Shprits, S. N. Walker, L. Chen, N. Cornilleau-Wehrin, I. Dandouras, O. Santolik, C. Carr, K. H. Yearby, and B. Weiss (2015), Observations of discrete harmonics emerging from equatorial noise, *Nat. Commun.*, *6*, 7703, doi:10.1038/ncomms8703.
 Bernstein, I. B. (1958), Waves in a plasma in a magnetic field, *Phys. Rev.*, *109*, 10–21, doi:10.1103/PhysRev.109.10.

- Boardsen, S. A., D. L. Gallagher, D. A. Gurnett, W. K. Peterson, and J. L. Green (1992), Funnel-shaped, low-frequency equatorial waves, *J. Geophys. Res.*, *97*, 14,967–14,976, doi:10.1029/92JA00827.
- Boardsen, S. A., G. B. Hospodarsky, C. A. Kletzing, R. F. Pfaff, W. S. Kurth, J. R. Wygant, and E. A. MacDonald (2014), Van Allen Probe observations of periodic rising frequencies of the fast magnetosonic mode, *Geophys. Res. Lett.*, *41*, 8161–8168, doi:10.1002/2014GL062020.
- Bortnik, J., and R. M. Thorne (2010), Transit time scattering of energetic electrons due to equatorially confined magnetosonic waves, *J. Geophys. Res.*, *115*, A07213, doi:10.1029/2010JA015283.
- Chen, L. (2015), Wave normal angle and frequency characteristics of magnetosonic wave linear instability, *Geophys. Res. Lett.*, *42*, 4709–4715, doi:10.1029/2015GL064237.
- Chen, L., R. M. Thorne, V. K. Jordanova, and R. B. Horne (2010), Global simulation of magnetosonic waves instability in the storm time magnetosphere, *J. Geophys. Res.*, *115*, A11222, doi:10.1029/2010JA015707.
- Chen, L., A. Maldonado, J. Bortnik, R. M. Thorne, J. Li, L. Dai, and X. Zhan (2015), Nonlinear bounce resonances between magnetosonic waves and equatorially mirroring electrons, *J. Geophys. Res. Space Physics*, *120*, 6514–6527, doi:10.1002/2015JA021174.
- Curtis, S. A., and C. S. Wu (1979), Gyroharmonic emissions induced by energetic ions in the equatorial plasmasphere, *J. Geophys. Res.*, *84*, 2597–2607, doi:10.1029/JA084iA06p02597.
- Fredricks, R. W. (1968), Structure of generalized ion Bernstein modes from the full electromagnetic dispersion relation, *J. Plasma Phys.*, *2*, 365–380, doi:10.1017/S002237780003895.
- Fu, H. S., J. B. Cao, Z. Zhima, Y. V. Khotyaintsev, V. Angelopoulos, O. Santolík, Y. Omura, U. Taubenschuss, L. Chen, and S. Y. Huang (2014), First observation of rising-tone magnetosonic waves, *Geophys. Res. Lett.*, *41*, 7419–7426, doi:10.1002/2014GL061867.
- Gary, S. P., K. Liu, D. Winske, and R. E. Denton (2010), Ion Bernstein instability in the terrestrial magnetosphere: Linear dispersion theory, *J. Geophys. Res.*, *115*, A12209, doi:10.1029/2010JA015965.
- Gulelmi, A. V., B. I. Klaine, and A. S. Potapov (1975), Excitation of magnetosonic waves with discrete spectrum in the equatorial vicinity of the plasmopause, *Planet. Space Sci.*, *23*, 279–286, doi:10.1016/0032-0633(75)90133-6.
- Gurnett, D. A. (1976), Plasma wave interactions with energetic ions near the magnetic equator, *J. Geophys. Res.*, *81*, 2765–2770, doi:10.1029/JA081i016p02765.
- Horne, R. B., G. V. Wheeler, and H. S. C. K. Alleyne (2000), Proton and electron heating by radially propagating fast magnetosonic waves, *J. Geophys. Res.*, *105*, 27,597–27,610, doi:10.1029/2000JA000018.
- Horne, R. B., R. M. Thorne, S. A. Glauert, J. M. Albert, N. P. Meredith, and R. R. Anderson (2005), Timescale for radiation belt electron acceleration by whistler mode chorus waves, *J. Geophys. Res.*, *110*, A03225, doi:10.1029/2004JA010811.
- Horne, R. B., R. M. Thorne, S. A. Glauert, N. P. Meredith, D. Pokhotelov, and O. Santolík (2007), Electron acceleration in the Van Allen radiation belts by fast magnetosonic waves, *Geophys. Res. Lett.*, *34*, L17107, doi:10.1029/2007GL030267.
- Li, J., et al. (2014), Interactions between magnetosonic waves and radiation belt electrons: Comparisons of quasi-linear calculations with test particle simulations, *Geophys. Res. Lett.*, *41*, 4828–4834, doi:10.1002/2014GL060461.
- Li, X., X. Tao, Q. Lu, and L. Dai (2015), Bounce resonance diffusion coefficients for spatially confined waves, *Geophys. Res. Lett.*, *42*(22), 9591–9599, doi:10.1002/2015GL066324.
- Liu, K., S. P. Gary, and D. Winske (2011), Excitation of magnetosonic waves in the terrestrial magnetosphere: Particle-in-cell simulations, *J. Geophys. Res.*, *116*, A07212, doi:10.1029/2010JA016372.
- Lu, Q., L. Zhou, and S. Wang (2010), Particle-in-cell simulations of whistler waves excited by an electron κ distribution in space plasma, *J. Geophys. Res.*, *115*, A02213, doi:10.1029/2009JA014580.
- Ma, Q., W. Li, R. M. Thorne, and V. Angelopoulos (2013), Global distribution of equatorial magnetosonic waves observed by THEMIS, *Geophys. Res. Lett.*, *40*, 1895–1901, doi:10.1002/grl.50434.
- Meredith, N. P., R. B. Horne, and R. R. Anderson (2008), Survey of magnetosonic waves and proton ring distributions in the Earth's inner magnetosphere, *J. Geophys. Res.*, *113*, A06213, doi:10.1029/2007JA012975.
- Němec, F., O. Santolík, K. Gereová, E. Macúšová, Y. de Conchy, and N. Cornilleau-Wehrin (2005), Initial results of a survey of equatorial noise emissions observed by the Cluster spacecraft, *Planet. Space Sci.*, *53*, 291–298, doi:10.1016/j.pss.2004.09.055.
- Němec, F., O. Santolík, Z. Hrbáčková, and N. Cornilleau-Wehrin (2015a), Intensities and spatiotemporal variability of equatorial noise emissions observed by the Cluster spacecraft, *J. Geophys. Res. Space Physics*, *120*, 1620–1632, doi:10.1002/2014JA020814.
- Němec, F., O. Santolík, Z. Hrbáčková, J. S. Pickett, and N. Cornilleau-Wehrin (2015b), Equatorial noise emissions with quasiperiodic modulation of wave intensity, *J. Geophys. Res. Space Physics*, *120*, 2649–2661, doi:10.1002/2014JA020816.
- Olsen, R. C., S. D. Shawhan, D. L. Gallagher, C. R. Chappell, and J. L. Green (1987), Plasma observations at the Earth's magnetic equator, *J. Geophys. Res.*, *92*, 2385–2407, doi:10.1029/JA092iA03p02385.
- Perraut, S., A. Roux, P. Robert, R. Gendrin, J. Sauvaud, J. Bosqued, G. Kremser, and A. Korth (1982), A systematic study of ULF waves above F/H+ from GEOS 1 and 2 measurements and their relationships with proton ring distributions, *J. Geophys. Res.*, *87*, 6219–6236, doi:10.1029/JA087iA08p06219.
- Russell, C. T., R. E. Holzer, and E. J. Smith (1970), OGO 3 observations of ELF noise in the magnetosphere. 2. The nature of the equatorial noise, *J. Geophys. Res.*, *75*, 755–768, doi:10.1029/JA075i004p00755.
- Santolík, O., J. S. Pickett, D. A. Gurnett, M. Maksimovic, and N. Cornilleau-Wehrin (2002), Spatiotemporal variability and propagation of equatorial noise observed by Cluster, *J. Geophys. Res.*, *107*, 1495, doi:10.1029/2001JA009159.
- Thorne, R. M., et al. (2013), Rapid local acceleration of relativistic radiation-belt electrons by magnetospheric chorus, *Nature*, *504*, 411–414, doi:10.1038/nature12889.
- Tsurutani, B. T., B. J. Falkowski, J. S. Pickett, O. P. Verkhoglyadova, O. Santolík, and G. S. Lakhina (2014), Extremely intense ELF magnetosonic waves: A survey of polar observations, *J. Geophys. Res. Space Physics*, *119*, 964–977, doi:10.1002/2013JA019284.
- Xiao, F., C. Yang, Z. Su, Q. Zhou, Z. He, Y. He, D. N. Baker, H. E. Spence, H. O. Funsten, and J. B. Blake (2015), Wave-driven butterfly distribution of Van Allen belt relativistic electrons, *Nat. Commun.*, *6*, 8590, doi:10.1038/ncomms9590.
- Zhima, Z., L. Chen, H. Fu, J. Cao, R. B. Horne, and G. Reeves (2015), Observations of discrete magnetosonic waves off the magnetic equator, *Geophys. Res. Lett.*, *42*, 9694–9701, doi:10.1002/2015GL066255.